Journal of Alloys and Compounds 509 (2011) 9876–9883

Contents lists available at ScienceDirect

Journal of Alloys and Compounds

journal homepage: www.elsevier.com/locate/jallcom

Variation of age-hardening behavior of TM-addition Al–Mg–Si alloys

Shumei Wang[a], Kenji Matsuda[b,*], Tokimasa Kawabata[b], Toshinari Yamazaki[b], Susumu Ikeno[b]

[a] Graduate School of Science and Engineering for Education, University of Toyama, Gofuku, Toyama, Japan
[b] Graduate School of Science and Engineering for Research, University of Toyama, Gofuku, Toyama, Japan

ARTICLE INFO

Article history:
Received 20 October 2010
Accepted 21 July 2011
Available online 28 July 2011

Keywords:
Transition metals
Al–Mg–Si alloy
Age hardening
Transmission electron microscopy
Dispersoid
Precipitate

ABSTRACT

Microstructure and aging hardness variation of Al–Mg–Si–TM alloys (TM = Co, Ni, Cr, Mn and Fe) were investigated to reveal the effect of transition metals (TMs) on the age hardening behavior of Al–Mg–Si alloy using transmission electron microscopy. The peak hardness of Co- or Ni-addition alloys is higher than the base alloy; Fe- or Cr-addition alloys is similar to the base alloy but Mn-addition alloy is lower than the base alloy. It was found different TM formed the dispersoids with different amounts of Si, which results in the different densities of the precipitates in different alloys. Si is expensed to form the dispersoid of Al(TM)Si for Cr-, Mn- and Fe-addition alloys. The ratio of TM:Si calculated from the EDS result of the dispersoid is the largest for Fe- and smallest for Mn-addition alloys. On the other hand, Si is not expensed to form such dispersoid in Co- and Ni-addition alloys. It is thought that this will result in the difference of Si in the matrix for the formation of the precipitate.

1. Introduction

In the continuing requirement for automobile weight reduction, the 6000 series Al–Mg–Si alloys has been considered as the promising candidates for age-hardenable bodysheet materials [1]. Transition metals (TMs) such as Cr, Fe and Mn, are usually added to Al alloys for grain refinement [2–4]. But these TMs will easily form some dispersoids during casting and heat treatment process [5,6].

According to Terai and Baba [7], Cr and Mn affect to the electrical conductivity of Al–Mg–Si alloy for extruded, annealed and even aged samples. It seems that Cr and Mn are more stable to remain in the matrix as solute elements than other elements, in addition to make insoluble intermetallic compounds as Al–Si–TMs. But the effect of the additional elements on the microstructure of these series alloys was not caused enough attention before. The effect of Cr and Fe addition on the age-hardening behavior of 6000 series alloys is reported by Matsuda et al. [8]. They indicated that (Cr + Fe)-bearing alloys included AlSi(CrFe) and AlSiFe dispersoids, which decreased the number density of precipitates and the aging effect of Si. On the contrary, Laughlin and Miao [9] reported an investigation of the effect of Mn content on the aging kinetics of Al alloys based on the 6022 composition and got the conclusion that the Mn level had very little effect on the peak hardness which developed in the 6022 variants. On the other hand, TMs, such as Co and Ni, commonly form the compounds of Al(TM) according to Al–TM–Mg or Al–TM–Si ternary phase diagram [10].

Several transition metals, i.e. Co, Ni, Cr, Fe and Mn are taken as the additional metals for Al–Mg–Si alloys in this work. The aim of this work is to focus on the following issues: (1) the variation of aging hardness for the alloys with different TMs addition, (2) the difference of the dispersoids formed with TMs addition, and (3) the effect of TMs on the activation energy for precipitation in the alloys. With this purpose in mind, hardness test, transmission electron microscopy (TEM), high resolution transmission electron microscopy (HRTEM) and differential scanning calorimetry (DSC) are used to determine these properties of Al–Mg–Si alloys with different transition metals addition.

2. Experimental

The quasi-binary alloy of Al–1.06Mg_2Si (at.%) is usually called as the base alloy for Al–Mg–Si ternary alloy. In this work, the TM-addition alloys (at.%) of Al–1.06Mg_2Si–0.2TM (TM = Co, Ni, Cr, Mn and Fe) were prepared by laboratory casting. They were melting in air using 99.99% pure Al, 99.9% pure Mg, 99.9% pure Si, and 99.9% pure TMs. The composition analysis of the obtained alloy is given in Table 1. The samples for Vickers hardness and TEM (HRTEM) observation were solution heat treated at 848 K for 3.6 ks in a circulating air furnace, cold water quenched, and followed by the artificial aging treatments at 473 K for different periods of time. The samples for DSC test were solution heat treated at 823 K.

Vickers hardness was measured using Akashi MVK-EII hardness tester (load: 0.98 N, holding time: 15 s). The hardness values reported here represent the average of at least ten measurements. TEM (HRTEM) observation was performed using Topcon EM-002B equipped with an energy dispersive X-ray spectroscopy (EDS). The accelerating voltage was 120 kV. Differential scanning calorimetry (DSC) test was taken with SII SSC/5200.

* Corresponding author. Tel.: +86 76 445 6839; fax: +81 76 445 6839.
E-mail addresses: matsuda@eng.u-toyama.ac.jp, wangshumei@hotmail.com (K. Matsuda).

0925-8388/$ – see front matter © 2011 Elsevier B.V. All rights reserved.
doi:10.1016/j.jallcom.2011.07.067

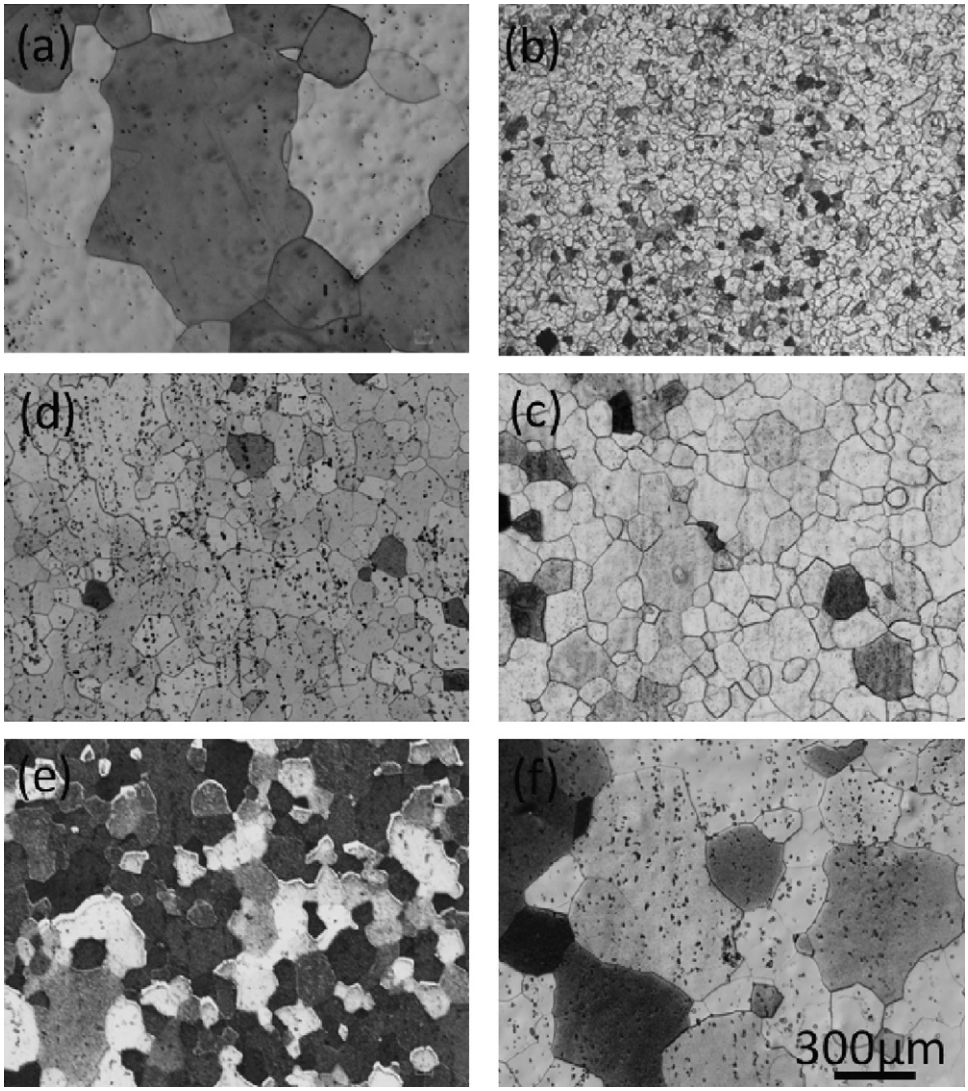

Fig. 1. Optical micrographs of the alloys with different TMs addition: (a) base, (b) Mn-addition, (c) Cr-addition, (d) Fe-addition, (e) Co-addition alloy and (f) Ni-addition alloys.

3. Results

Fig. 1 shows the optical micrographs of the alloys with different TMs addition. The grain size is calculated as 649, 40, 64, 91, 57 and 174 μm for different alloys, as shown in Table 1. The grain size of TM-addition alloys is much smaller than the base alloy, which is resulted from the grain refinement effect of TM addition. Fig. 2 shows the variation of the micro Vickers hardness for the alloys aged at 473 K, which is plotted as a function of aging time. The as-quenched hardness of the TM-addition alloys is higher than the base alloy because of the smaller grains formed in TM-addition alloys. The peak hardness of Co- or Ni-addition alloy is higher than the base alloy. The peak hardness of Cr- or Fe-addition alloy is similar to the base alloy. The peak hardness of Mn-addition alloy, however, is much lower than the base alloy. This result is supported by our previous work [8] but different with Laughlin and Miao [9]. The reason for the difference with Laughlin and Miao is properly caused by the difference of the chemical composition between the alloys used in this work and [9], in which the existence of 1.0 mass% ex.Si for the alloy including Cu is enough to form the precipitates that affect the age hardening behavior of the alloy.

The six alloys peak-aged at 473 K are taken to examine the difference of the precipitates distribution in this work. The TEM bright-field images are displayed in Fig. 3. There are only needle-shaped precipitates aligning with $\langle 1\,0\,0\rangle_{Al}$ direction for the six alloys. The number density of these precipitates can be calculated as 146, 37, 150, 157, 261 and 359 μm^{-2} for the base, Mn-, Cr-, Fe-,

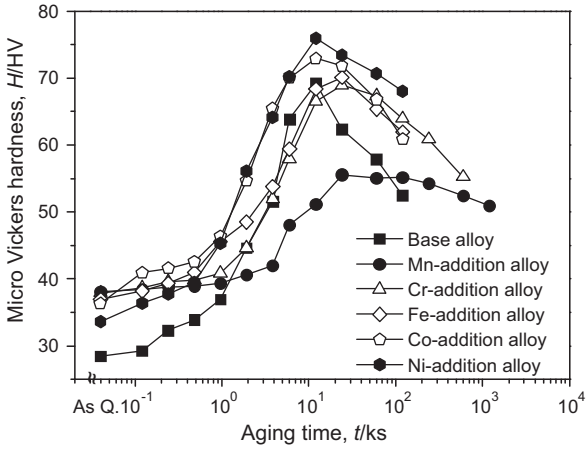

Fig. 2. Micro Vickers hardness curves of six alloys aged at 473 K.

Table 1
Composition analysis result of the alloys used in this work (at.%).

Alloys	Mg	Si	Fe	Cu	Mn	Cr	Zn	Ni	Co	Al	Grain size (μm)
Base alloy	0.71	0.37	<0.01	<0.01	<0.01	0.00	<0.01	0.00	0.00	bal.	649
Mn-addition alloy	0.75	0.31	<0.01	<0.01	0.24	<0.01	<0.01	0.00	0.00	bal.	40
Cr-addition alloy	0.72	0.36	<0.01	<0.01	<0.01	0.19	<0.01	0.00	0.00	bal.	64
Fe-addition alloy	0.67	0.32	0.16	<0.01	<0.01	0.00	<0.01	0.00	0.00	bal.	91
Co-addition alloy	0.69	0.33	<0.01	<0.01	<0.01	0.00	<0.01	0.00	0.18	bal.	57
Ni-addition alloy	0.71	0.36	<0.01	<0.01	<0.01	0.00	<0.01	0.18	0.00	bal.	174

Co- and Ni-addition alloys, respectively. The number density of the precipitates for Mn-addition alloy is much lower than the other alloys, which is attributed to one of the reason why its peak hardness is much lower than the other alloys. The difference between the peak hardness and the as-quenched hardness is described as ΔHV. The variation of ΔHV according to the number density of the precipitates (N) is shown in Fig. 4a. The square root of number density of the precipitates, $N^{1/2}$, for every alloy was calculated and it was normalized to divide the value $N^{1/2}$ of Ni-addition alloy, as L^{-1}. The variation of ΔHV against L^{-1} is shown in Fig. 4b. There is a

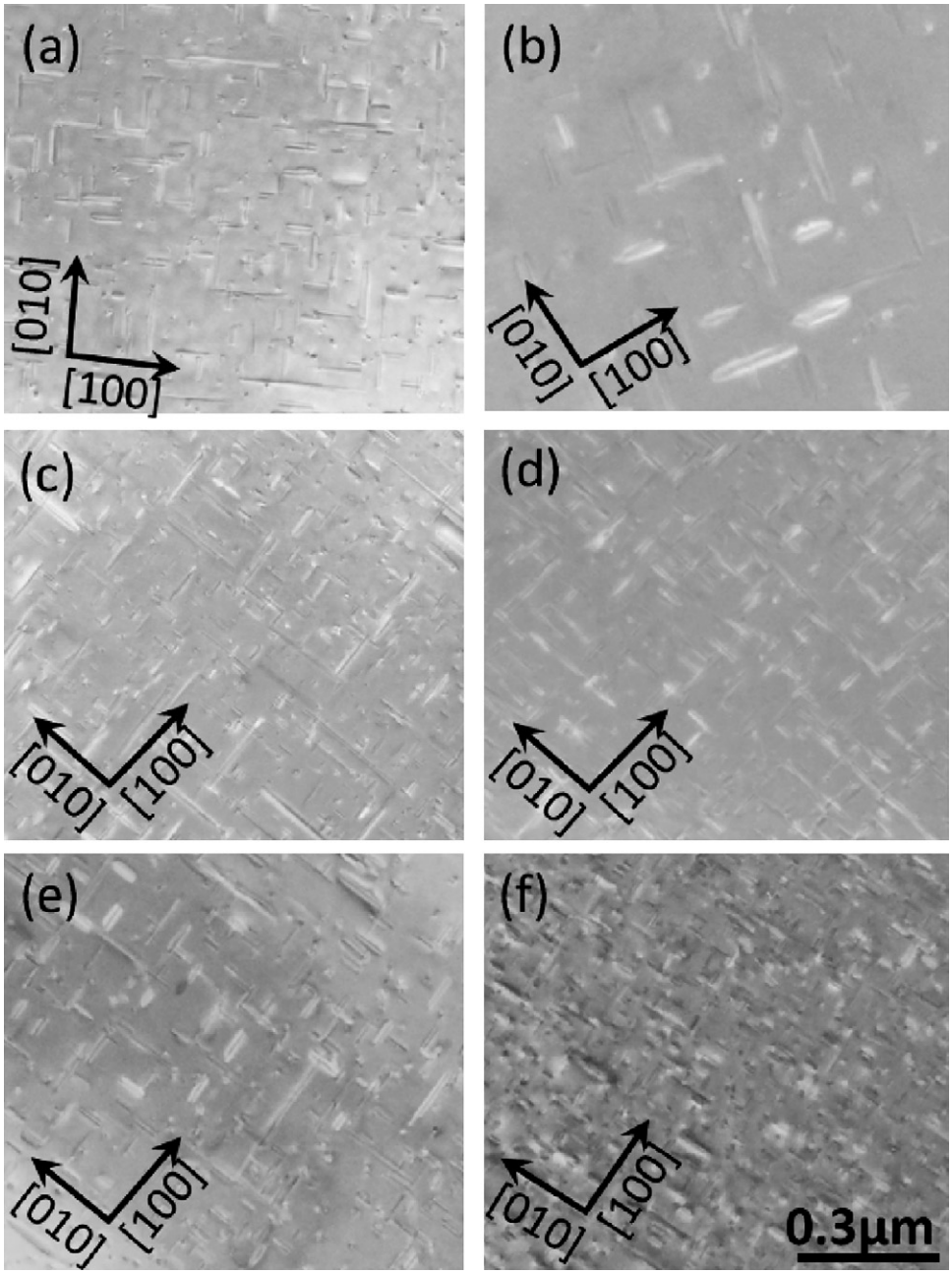

Fig. 3. TEM bright-field images of the alloys with different TMs addition: (a) base, (b) Mn-addition, (c) Cr-addition, (d) Fe-addition, (e) Co-addition alloy and (f) Ni-addition alloys.

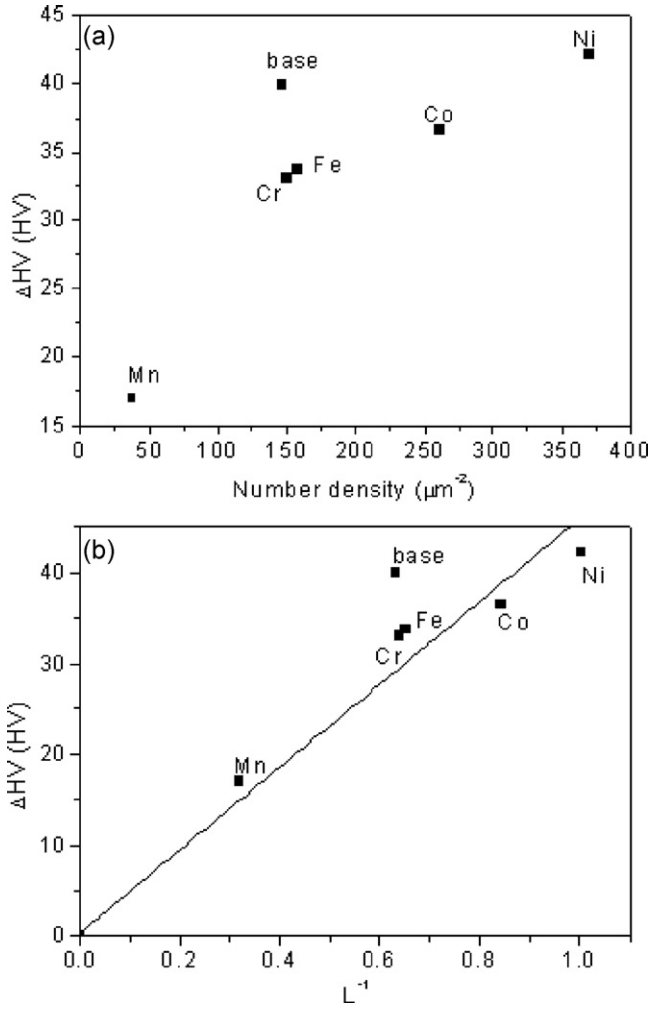

Fig. 4. Variation of ΔHV according to (a) the number density and (b) L^{-1}.

linear relationship between two parameters, which is though as the mechanism for the effect of the precipitates on the motion of dislocation, $\tau \propto L^{-1}$, where τ is the applied stress and L is the average distance between the particles [11].

HRTEM observation was taken for base, Ni-, Co-, Fe- and Mn-addition alloys. The HRTEM images taken from the cross-section of the predominated precipitates in Co-, Fe- and Mn-addition alloys are shown in Fig. 5. Fig. 5a shows the precipitate in Co-addition alloy with the parallelogram networks of the bright dots with the interior angle fixed to 75°. It can be attributed to the β″ phase [12]. The predominant precipitate formed in Ni-addition alloy is as the same as Co-addition alloy. Fig. 5b also shows the precipitate in Fe-addition alloy with the parallelogram networks of the bright dots. Its interior angle (θ) is not fixed to a certain degree but spans the range of $60° < \theta < 90°$. It can be attributed to the parallelogram-type precipitate [13]. The hexagonal networks of the bright dots of the precipitate in Mn-addition alloy are observed in Fig. 5c with the spacing about 0.7 nm, and the direction of the precipitate (indicated as P) is inclined by 10° to the $\langle 1\,0\,0\rangle_{Al}$ direction of the matrix which is similar to the data shown in [14,15] for the β′ phase. The random-type precipitate [16] cannot be observed as the predominant precipitate for TM-addition alloys. The corresponding distribution of every precipitate in different alloys is shown in Fig. 6 with the decreasing order of the peak hardness from the top to the bottom. The distribution of the precipitates for the base alloy has been reported in our previous work [13]. The random-type and parallelogram-type precipitates are observed as

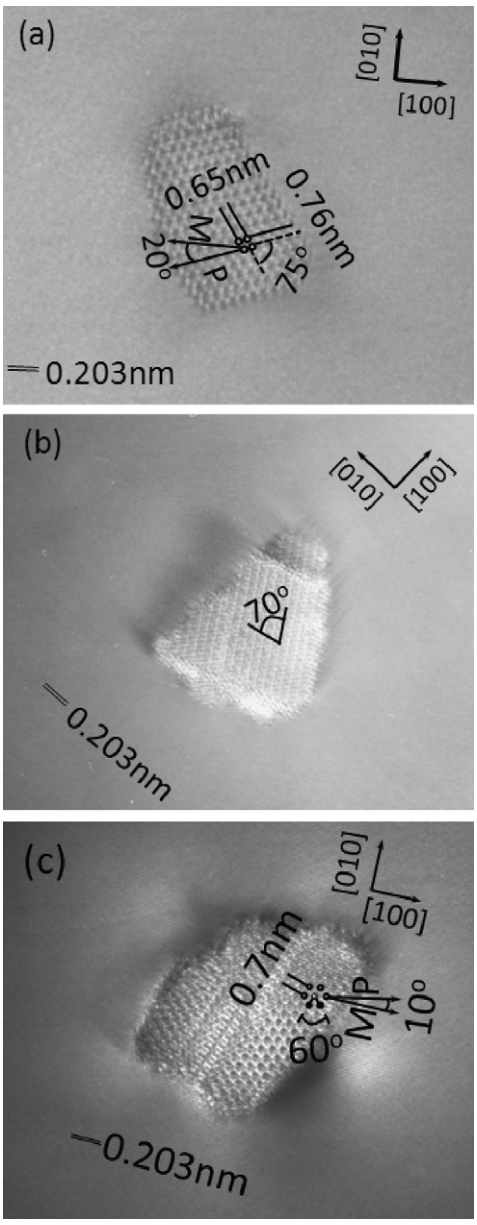

Fig. 5. HRTEM images of the predominated precipitates in (a) Co-, (b) Fe- and (c) Mn-addition alloys.

the main precipitates in the base alloy. It means that the precipitation sequence for four TM-addition alloys is shifted to more stable phases than the base alloy because the random-type precipitates are formed between GP zone and parallelogram-type precipitate, β″ or β′ phase according to our previous report [17].

The grain boundary precipitates have also been examined to investigate whether these precipitates contain TM or not because the grain boundary precipitates are generally larger and more stable than the precipitates in the matrix. Fig. 7 shows TEM bright- and dark-field images of the precipitates formed in the matrix and the grain boundary of Mn-addition alloy. There are two crystal grains shown in the left and right sides of Fig. 7. The bright dots shown in Fig. 7b are the grain boundary precipitates observed arranging align of the grain boundary. These bright dots are the cross-section of the rod-shape precipitates and are parallel to [0 0 1] of the matrix direction as the same as the precipitates in the left crystal grain. A precipitate free zone can be seen around the grain boundary. A typical HRTEM image of the grain boundary precipitate is shown by

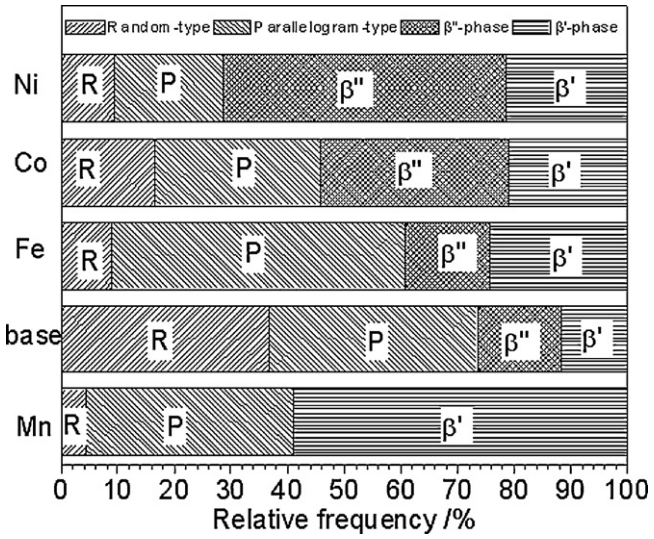

Fig. 6. Relative frequency of the precipitates in five alloys.

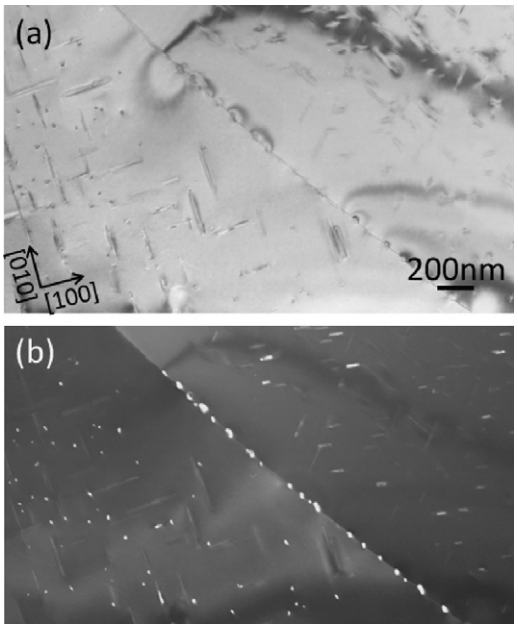

Fig. 7. TEM bright-field (a) and dark-field (b) images of the precipitates in the matrix and the grain boundary.

Fig. 8a. The arrangement of the bright dots is similar to the precipitate shown in Fig. 5c. Only Al, Mg and Si peaks are detected from these precipitates according to the EDS spectrum (Fig. 8b). Mn is not detected in this precipitate. Fig. 8c shows the SAED pattern taken from the same precipitate and Fig. 8d is the simulation of the SAED pattern. If this crystal lattice is hexagonal and it has $a = 0.705$ and $c = 0.405$ nm, the spacing of the crystal plane calculated by d1 and d2 in Fig. 8d are 0.35 nm for {1 1 2 0} and 0.63 nm for {1 1 0 0} planes of β′ phase. Therefore, this precipitate is attributed to β′ phase in this work and the β′ phase formed in the grain boundary here does not contain Mn.

It has been well known that Mn, Cr or Fe will form the dispersoids of Al(TM)Si with the inhomogeneous distribution. The dispersoids are observed in five TM-addition alloys in this work.

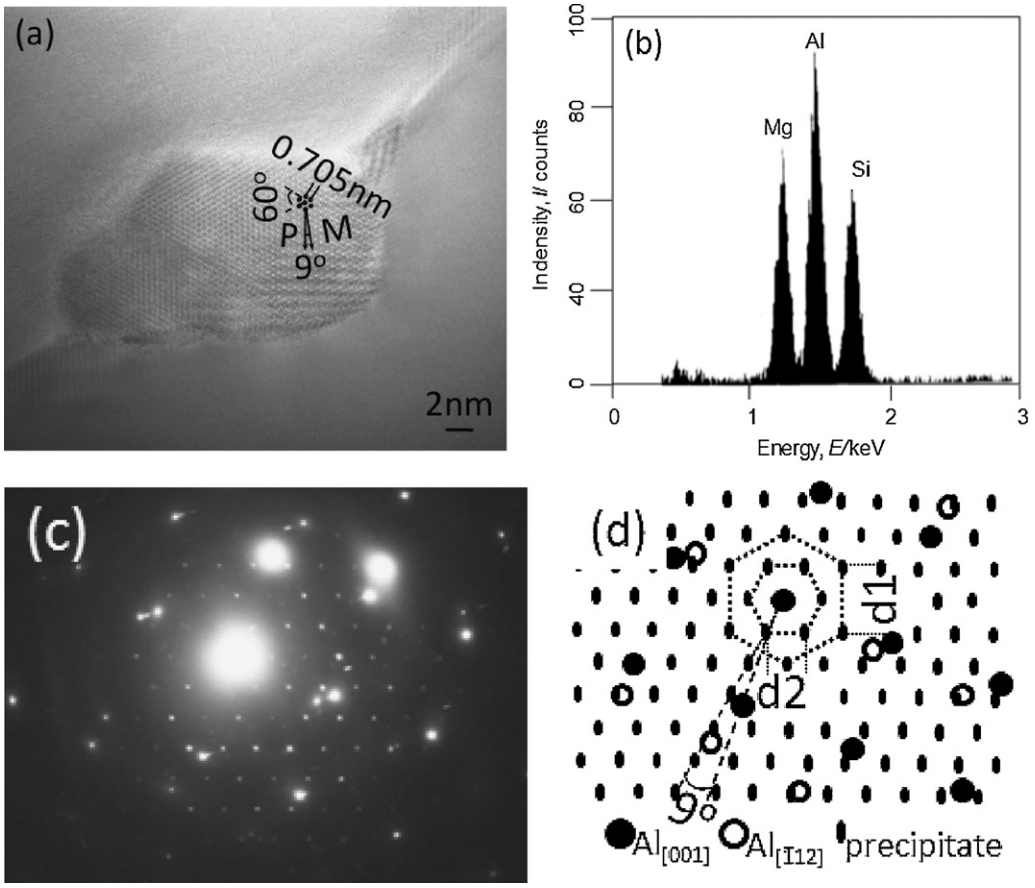

Fig. 8. Precipitate in grain boundary: (a) HRTEM image, (b) EDS spectrum, (c) SAED pattern and (d) simulation of (c).

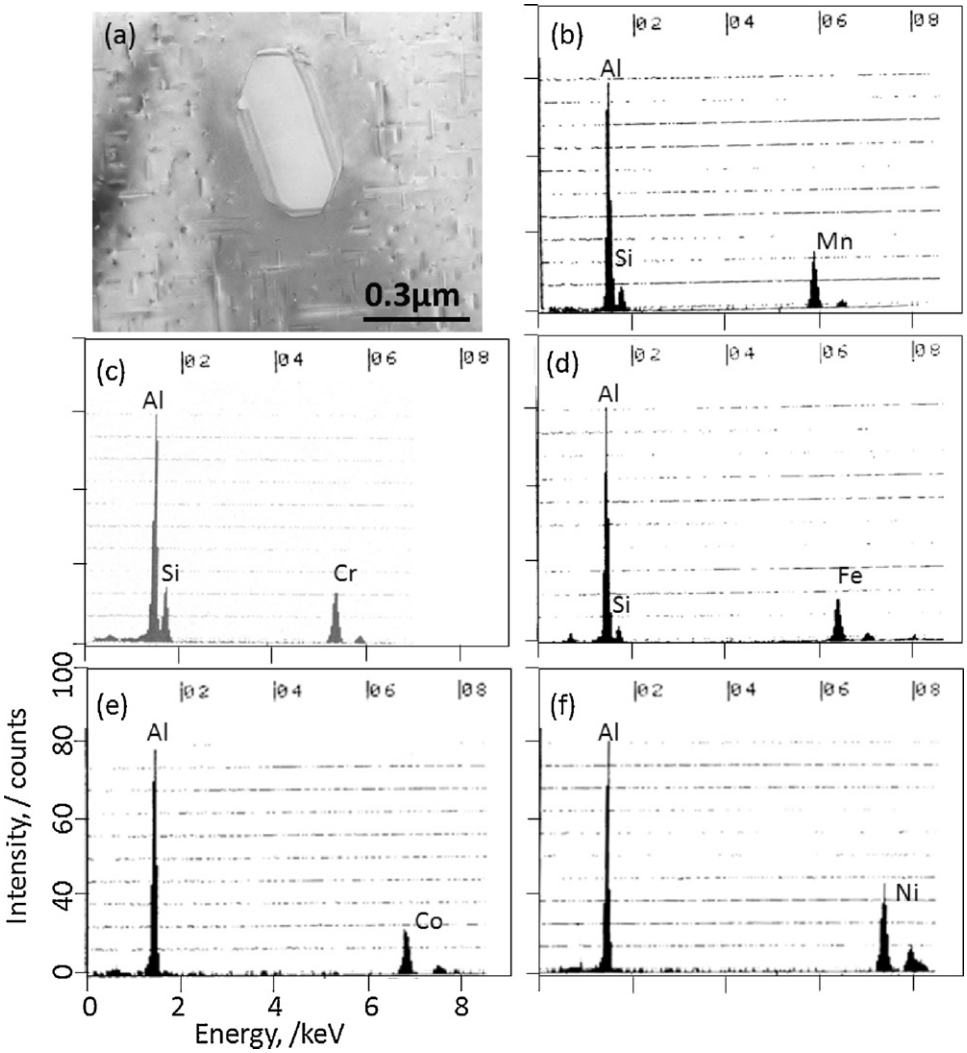

Fig. 9. (a) TEM image of the dispersoid formed in Cr-addition alloy, (b)–(e) EDX spectrum of the disperoids formed in different TM-addition alloy.

Fig. 9a shows the TEM bright-field image, which is taken from the dispersoid formed in Cr-addition alloy as an example. The size of the dispersoid is much larger than the precipitates. And there is a precipitate free zone around the dispersoid. Fig. 9b–e shows the EDS spectrum of the dispersoids formed in different TM-addition alloys. Al, Si, and TM peaks are detected for Mn-, Cr- and Fe-addition alloys (Fig. 9b–d). The ratio of TM:Si is determined using Cliff–Lorimer method shown in Fig. 10 with respect to Al (i.e. the matrix) [18]. The TM:Si ratio is calculated as 1.5, 1.7 and 2.1 for the dispersoids formed in Mn-, Cr- and Fe-addition alloys, respectively. The ratio of TM:Si obtained in this work is similar to the dispersoids of $Al_{15}Mn_3Si_2$ [19] (or $Al_{12}Mn_3Si_2$ [20]), Al_8Fe_2Si [21] and $Al_{8.9}Cr_4Si_{2.1}$ [22] reported before. Only Al and TM peaks are detected for Co and Ni-addition alloys (Fig. 10e and f). That is to say, Si is not expensed for the formation of the dispersoids in Co- and Ni-addition alloys.

4. Discussion

DSC is a well-established technique which has been utilized to characterize precipitate microstructures and kinetics rapidly in age-hardenable aluminum alloys [23]. DSC scans are performed for TM-addition alloys. Fig. 11 shows the DSC curve scanning at 20 K/min for Co-addition as an example. Seven reaction peaks in DSC scans are usually occurring for TM-addition alloys: five are exothermic reactions, labeled as I, II, IV, V and VII; and two are endothermic reactions, labeled as III and VI. The exothermic reaction peaks I, II, IV, V and VII corresponds to the formation of clusters, Guinier–Preston (GP) zone, β″, β′ and β phase [24]. And the endothermic reaction peaks III and VI corresponds to the dissolution of the precipitates. The activation energy for the formation of the β′ phase were calculated by Kissinger method [25] using peak IV on DSC curves and summarized in Table 2 for every TM-addition alloy. This table also includes the activation energy calculated from the hardness curves of every alloy using Johnson–Mehl–Avrami equation [26]. The Mn-addition alloy shows the lowest activation energy for the formation of β′-phase than other alloys. It is in good agreement with the peak hardness. As mentioned before, the relative content of Si expensed for the formation of the dispersoids is the highest for Mn-addition alloy. So Si for the formation of homogeneous precipitates becomes small and the formation of the precipitates will decrease in this alloy. The lowest activation energy for the formation of the β′ phase means that it is easier to form

Table 2
Activation energy (kJ/mol) for the formation of β′-phase calculated from DSC and hardness curves.

Calculated by	base	Mn	Cr	Fe	Co	Ni
Hardness	107.9	61.2	71.2	73.2	81.5	66.0
DSC	95.9	55.7	74.9	63.0	82.6	69.4

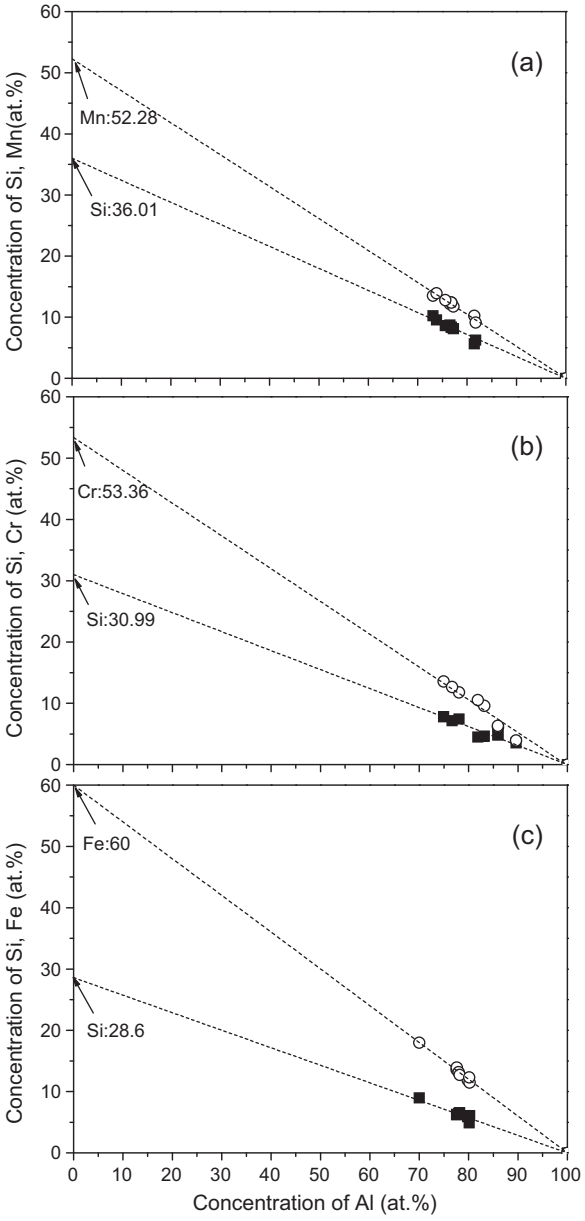

Fig. 10. Determination of the ralative ratio of TM:Si for the dispersoids obtained in (a) Mn-, (b) Cr- and (c) Fe-addition alloys using the Cliff–Lorimer method.

β′ phase in Mn-addition alloy. The reason is explained as that the interface between the dispersoid and the matrix acts as the sink of the quenched-in vacancy. The absence of supersaturation of solute atoms for the nucleation furthermore results in the decrease of the precipitates in Mn-addition alloy. The ratio of TM:Si is different for the alloys with Cr, Mn and Fe addition, as shown in Fig. 10. Si expended for the dispersoids is the highest for Mn-addition alloy and the lowest for Fe-addition alloy. Si is not expensed for the dispersoids in Co- and Ni-addition alloy. This results in Si for the formation of the precipitates in the matrix is the most for Co- and Ni-addition, while the less for Mn-addition alloy. Therefore, the inhomogeneous precipitation of the metastable phase is probably promoted by these two reasons shown here.

The bond overlap population (BOP) value by discrete-variational (*DV*)–*Xa* method using the BONDODR program [27] was calculated using the cluster indicated in Fig. 12 which include some Si and TM elements and summarized in Table 3 as the relationship with the ratio of Si:TM for the dispersoids reported before. Dispersoids of Al(TM)Si is thought to be formed easier for Cr-, Mn- and Fe-addition alloy because the BOP value of them is larger than Co- and Ni-addition alloy. As mentioned in Section 1, TMs, Co and Ni, commonly form the compounds of AlTM not form Al(TM)Si dispersoids like Cr, Fe and Mn after adding to Al–Mg–Si alloy according to Al–TM–Mg or Al–TM–Si ternary phase diagram. This keeps assistance with the BOP result calculated in this work.

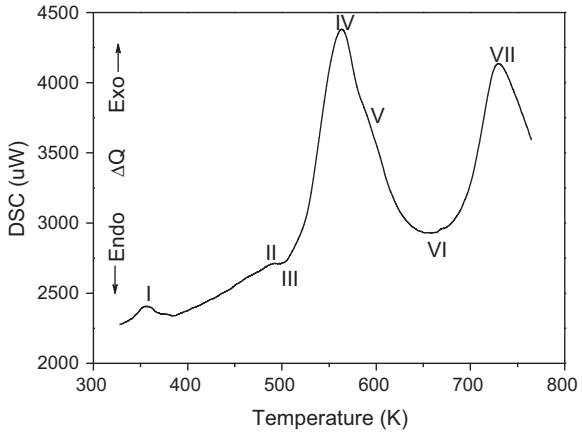

Fig. 11. DSC curves Co-addition alloys with the heating speed of 20 K/min.

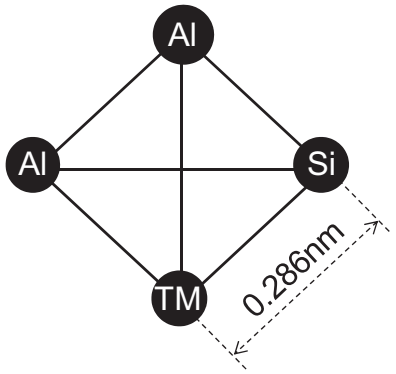

Fig. 12. Cluster model for the calculation of BOP.

Table 3
Si:TM ratio and BOP value for the alloys with different TM.

TM	Cr	Mn	Fe	Co	Ni
Si:TM	0.52	0.67	0.5	0	0
BOP	0.406	0.387	0.367	0.336	0.307

5. Conclusions

The grain refinement effect of TMs causes the grain size of the TM-addition alloys smaller than the base alloy, which results in the increase of the as-quenched hardness for the TM-addition alloys.

The precipitates in five alloys peak-aged at 473 K are observed by HRTEM and classified for the random-type precipitate, parallelogram-type precipitate, β″ phase and β′ phase. The precipitation sequence for four TM-addition alloys is shifted to more stable phases, parallelogram-type precipitate, β″ phase and β′ phase, than the base alloy in which the random-type precipitate is observed as the main precipitate.

The peak hardness of Co- and Ni-addition alloys is higher, while the Mn-addition alloy is much lower than the base alloy. The Mn-addition alloy has the lowest activation energy for the formation of β′-phase among other alloys. It is in good agreement with the peak hardness.

The BOP result obtained in this work indicates that Al(TM)Si dispersoid is formed easier in Cr-, Mn- and Fe-addition alloys than in Co- and Ni-addition alloys.

Acknowledgement

The authors thank to Dr. T. Okada, SUS corporation for supporting a part of this research.

References

[1] W.S. Miller, L. Zhuang, J. Bottema, A.J. Wittebrood, P.D. Smet, A. Haszler, A. Vieregge, Mater. Sci. Eng. A 280 (2000) 37–49.
[2] L.F. Mondolfo, Aluminum Alloys, Structure and Properties, Butterworth, London, 1976.
[3] Microstructure and Properties in Aluminum Alloys, J. Inst. Light Met. (1991) 289.
[4] H. Westengen, L. Auran, O. Reiso, Aluminum 12 (1981) 797–803.
[5] H. Tanihata, T. Sugawara, K. Matsuda, S. Ikeno, J. Mater. Sci. 34 (1999) 1205–1210.
[6] R.J. Livak, Metall. Trans. A 13 (1982) 1318–1321.
[7] S. Terai, Y. Baba, J. Jpn. Inst. Met. 13 (1963) 6–350 (in Japanese).
[8] K. Matsuda, K. Kido, S. Taniguchi, Y. Uetani, S. Ikeno, J. Jpn. Inst. Met. 52 (2002) 398–402 (in Japanese).
[9] D.E. Laughlin, W.F. Miao, Automotive Alloy II (1998) 63.
[10] P. Villar, A. Prince, H. Okamoto (Eds.), Handbook of ternary alloy phase diagrams (1995).
[11] B. Chalmers (Ed.), Progress in materials science, (1963) 300–333.
[12] K. Matsuda, T. Naoi, K. Fujii, Y. Uetani, T. Sato, A. Kamio, S. Ikeno, Mater. Sci. Eng. A 262 (1999) 232–237.
[13] K. matsuda, H. Gamada, K. Fujii, Y. Yoshida, T. Sato, A. Kamio, S. Ikeno, J. Jpn. Inst. Light Met. 47 (1997) 493–499 (in Japanese).
[14] K. Matsuda, S. Taba, S. Ikeno, J. Electron Microsc. 42 (1993) 1–4.
[15] K. Matsuda, S. Ikeno, S. Taba, J. Jpn. Inst. Metal 57 (1993) 1107–1113 (in Japanese).
[16] K. Matsuda, H. Gamada, K. Fujii, Y. Uetani, T. Sato, A. Kamio, S. Ikeno, Metall. Mater. Trans. A 29 (1998) 1161–1167.
[17] S. Ikeno, H. Matsui, K. Matsuda, K. Terayama, Y. Uetani, J. Jpn. Inst. Metal. 65 (2001) 404–408.
[18] G. Cliff, G.W. Lorimer, J. Microsc. 103 (1975) 203–207.
[19] N.A. Belov, D.G. Eskin, A.A. Aksenov, Multicomp. Phase Diag. Appl. Commercial Aluminum Alloys (2005) 12–15.
[20] W. Eidhed, H. Tezuka, T. Sato, J. Mater. Sci. Technol. 24 (2008) 21–24.
[21] M.H. Mulazimoglu, A. Zaluska, J.E. Gruzleski, F. Paray, Metall. Mater. Trans. A 27 (1996) 929–936.
[22] F. Weitzer, H. Chen, Y. Du, J.C. Schuster, Intermetallics 14 (2006) 224–226.
[23] R. Deiasi, P.N. Adler, Met. Trans. A 8 (1977) 1177–1183.
[24] I. Dutta, S.M. Allen, J. Mater. Sci. Lett. 10 (1991) 323–326.
[25] H.E. Kissinger, J. Res. NBS 57 (1956) 217–221.
[26] J. Chriatian, The Theory of Transformation in Metals and Alloys-Part I, 2nd ed., Pergamon, Oxford, 1975.
[27] H. Adachi, Y. Owada, I. Tanaka, H. Nakamatsu, M. Mizuno, Introduction to DV-Xa Method, 3rd ed., Sankyo Shuppan Co., Ltd., Tokyo, 2001 (in Japanese).